Article

Optimizing the corrosion performance of rust layers: role of Al and Mn in lightweight weathering steel

Check for updates

Yihao Tang[1], Yuxing Guo[1], Pengfei Ji[1,2], Bo Li[1,2], Chaoqun Xia[3] ✉, Shuzhi Zhang[1], Junsong Zhang[1], Xinyu Zhang[1] ✉ & Riping Liu [1] ✉

In this study, the corrosion behavior of AlMn lightweight weathering steel (LWS) in the simulated marine atmosphere was investigated by means of the dry/wet corrosion cycle test. The results showed that Al was present as $FeAl_2O_4$ and enriched in the inner layer, which significantly optimizes the rust layer in terms of compactness, elemental distribution, phase constitution, and electrochemical properties. The Mn oxides promoted the formation of $FeAl_2O_4$ and enhanced the anti–rupture ability of the LWS's rust layer.

Weathering steel circumvents severe corrosion problems in the atmosphere by reducing the corrosion rate through the formation of a firmly adherent and protective rust layer[1–3]. Weathering steel is widely used in marine and land transportation industries, such as railway freight vehicles and containers, etc. However, the major alloying elements in weathering steel, Cu (ρ: 8.92 g cm^{-3}) and Ni (ρ: 8.91 g cm^{-3}), increase the density of the steel (~7.85 g cm^{-3}). The use of conventional weathering steel with high-density results in increased energy consumption and emissions during transportation. By contrast, the lightweight of weathering steel contributes to environmental relief. In the meantime, conventional weathering steel struggles to form a stable and protective rust layer in harsh atmospheres, resulting in severe corrosion. Therefore, developing low–density weathering steel with excellent corrosion resistance is necessary and urgent.

Fe–Al–Mn–C lightweight steel has received considerable attention due to its low density, and exceptional mechanical properties[4–9]. The addition of Al (ρ: 2.70 g cm^{-3}) alters the lattice parameters of steels, while simultaneously reducing density due to its low atomic mass. A density reduction of ~0.1 g cm^{-3} can be achieved per 1 wt% of Al[10]. Chen et al.[11] reported that the addition of Al improved the corrosion resistance of weathering steel in a simulated marine atmosphere. The inner rust layer structure was improved and anodic dissolution was inhibited by the presence of Al in the form of the spinel oxide $FeAl_2O_4$. Moreover, Al alloying increased the content of α-FeOOH and improved the protective properties of the rust layer. However, Xu et al.[12] concluded that although large size Al–enriched particles composed of AlOOH and Al(OH)$_3$ can fill in the cracks and pores in the rust layer

and improve corrosion resistance, they cannot block the invasion of Cl$^-$. Mn (ρ: 7.47 g cm^{-3}) enhances the strength and toughness of steel by solid solution strengthening, compensating for the partial loss of strength caused by reduced carbon concentration. In addition, Mn significantly reduces the ferrite transformation temperature and promotes austenite formation. Fajardo et al.[13] found that increasing Mn concentration in Fe-Al-Mn-Si steels had a negative impact on corrosion resistance due to the less protective Mn oxides in the surface film. However, Dae et al.[14] found that the corrosion resistance of Mg–4Zn–0.5Ca–xMn was improved by the addition of Mn, and that Mn oxides could block Cl$^-$ invasion. The form of Al present in the rust layer and the effect of Al and Mn on the corrosion resistance of alloy remains controversial. However, the corrosion behavior of AlMn weathering steel in the marine atmosphere is poorly understood. In particular, the synergistic mechanism of Al and Mn requires further exploration.

The work reported by this paper aims to explain the evolution of the rust structure, elemental distribution, phase composition, and corrosion resistance of lightweight weathering steel in a simulated marine atmosphere. The cross–sectional morphology of the rust layer was observed using scanning electron microscope (SEM), and the relevant element distribution was characterized by energy dispersive spectrometry (EDS). In addition, X–ray diffraction (XRD), Raman spectrometry, X–ray photoelectron spectroscopy (XPS), and transmission electron microscopy (TEM) were used to analyze the phase composition of the rust layer. Finally, the electrochemical properties of the rust layer were investigated by potentiodynamic polarization curve and electrochemical impedance spectroscopy (EIS).

[1]State Key Laboratory of Metastable Materials Science and Technology, Yanshan University, Qinhuangdao 066004, China. [2]Shandong Laboratory of Yantai Advanced Materials and Green Manufacture, Yantai 264006, China. [3]Tianjin Key Laboratory of Materials Laminating Fabrication and Interface Control Technology, School of Materials Science and Engineering, Hebei University of Technology, Tianjin 300130, China. ✉e-mail: chaoqunxia@hebut.edu.cn; xyzhang@ysu.edu.cn; riping@ysu.edu.cn

Results

Microstructure and mechanical properties

Figure 1a shows the microstructure of CWS, which comprises pearlite and ferrite. Meanwhile, Fig. 1b–d shows the microstructure of LWSs, wherein LWS1 comprises austenite, LWS2 comprises austenite and ferrite, and LWS3 comprises ferrite, correspondingly. The engineering stress-strain curves for LWSs are displayed in Fig. 2, and Table 1 exhibits the mechanical properties of the experimental steels. By adjusting the composition of LWS, it is possible to achieve superior mechanical properties than CWS. The addition of Al reduces the weldability of the steel, and due to the high Mn content, Mn vapor will be released when welding. The above–mentioned disadvantages of lightweight steel can be overcome by laser welding. Refinement of grain size can be achieved by adding alloying elements such as Ti/Nb, thus avoiding coarse grain structure. Increasing the melting temperature improves the fluidity of molten steel and avoids clogging.

Corrosion weight gain

Figure 3 shows the evolution of weight gain with time shown by the experimental weathering steels in the simulated marine atmosphere. Corrosion weight gain curves were fitted and the results are listed in Table 2. The weight gain of CWS was divided into two stages, with the slope of the second stage being smaller than that of the first stage. Throughout the test, the corrosion rate of CWS initially increased and then gradually decreased. The corrosion rate was closely related to the rust layer that had formed on the steel surface. The reduction in the corrosion rate of CWS indicated that the protective performance of the rust layer has gradually improved. The weight gains of LWS1 and LWS2 increased linearly. The weight gains of LWS1 and LWS2 were considerably lower than that of CWS, and the weight gain of LWS1 was always smaller than that of LWS2. The weight gain of LWS3 was also divided into two stages, with the slope of the second stage being larger than that of the first stage. The protective ability of the rust layer was significantly weakened in the later stage of the experiment. The rust layer of

LWS3 may be damaged with the progression of corrosion. The weight gain of LWS was much smaller than that of CWS, indicating that the rust layer of LWS is more protective and less prone to corrosion than that of CWS. The addition of Al significantly reduces the corrosion weight gain of weathering steel in the marine atmosphere and enhances its corrosion resistance. At the same time, higher Mn concentration results in a reduced corrosion weight of LWS, while preventing a sudden increase in corrosion weight gain during the later stage of corrosion.

Rust morphology and element distrubution

To provide a comprehensive view of the rust layer, cross-sections of experimental steels with different CCTs were observed, as shown in Fig. 4. Morphology analysis revealed that all rust layers have tightly adhered to the steel matrix. The rust layer thicknesses of 10CCT, 20CCT, and 30CCT of CWS were 94.23, 121.15, and 176.28 μm, respectively. Initially, the rust layer of CWS had a loose and porous structure. Cl^- and O_2 could easily penetrate the rust layer and could reach the steel matrix. Therefore, the corrosion rate was very high. As the experiment progressed, the rust layer on CWS thickened and compacted, resulting in a decrease in the corrosion rate. But there are a lot of holes and cracks in 30CCT. The rust layer on LWS1 was divided into a loose outer layer and a compact inner layer. The increase in CCT had minimal impact on the rust layer thickness and morphology of LWS1. The rust layer thickness of 30CCT was 31.60 μm, which only increased by 8.95 μm compared to 10CCT. The rust layer thickness of LWS2 and LWS1 were the same for 10CCT, but LWS2 had more transverse cracks than LWS1. As the experiment proceeded, the rust layer thicknesses of 20CCT and 30CCT of LWS2 were both larger than those of LWS1, and the thickness of 30CCT was 48.16 μm. There are more transverse cracks, but they are favorable for impeding Cl^- penetration and reducing the corrosion rate compared to longitudinal cracks. The rust layer of LWS2 still protected the matrix well because of its compact structure. The large difference in rust layer thickness and compactness indicated that the protective effect of LWS1

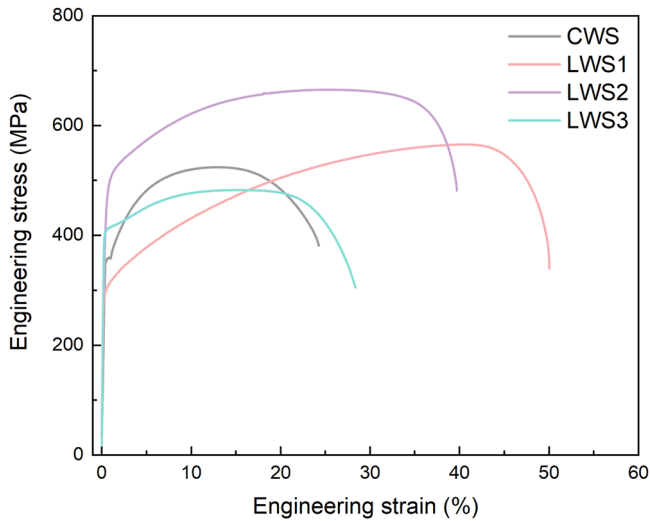**Fig. 1 | OM images. a** CWS, **b** LWS1, **c** LWS2 and **d** LWS3.
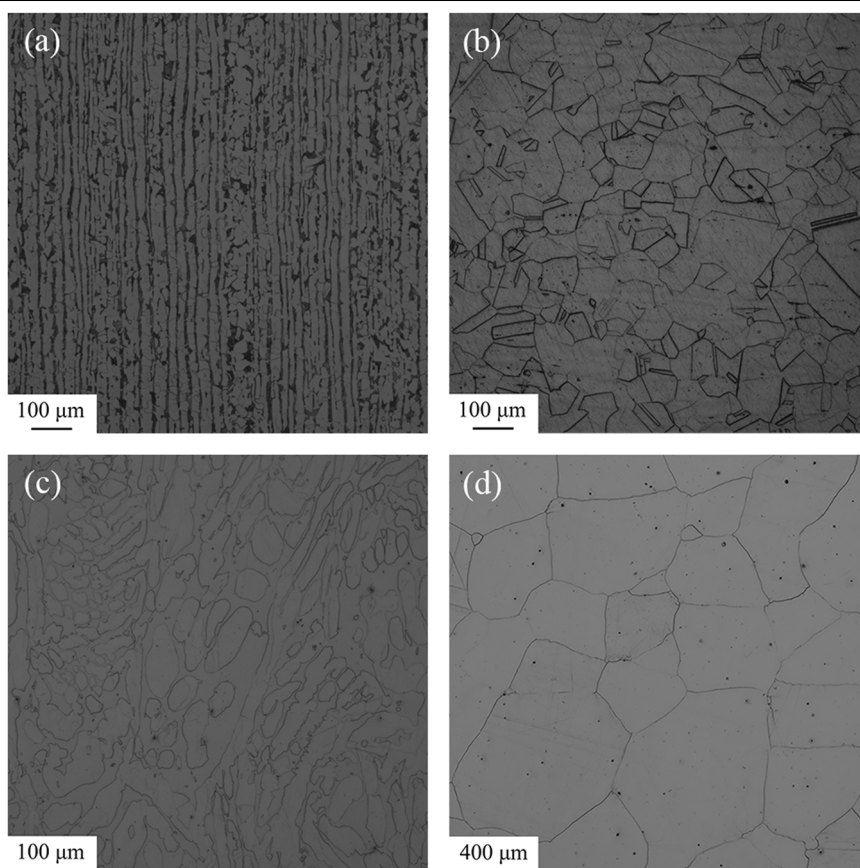
Fig. 2 | Engineering stress-strain curves of experimental steels.

Fig. 3 | Weight gain results of CWS and LWSs.

Table 1 | Mechanical properties of experimental steels

Steel	Yield strength (MPa)	Tensile strength (MPa)	Total elongation (%)
CWS	347	523	24.26
LWS1	295	565	50.04
LWS2	465	650	39.71
LWS3	406	482	28.36

Table 2 | Fitted results of weight gain curves

Steel	First stage	Second stage
CWS	$y = -0.08 + 0.78x$ ($0 \leq x \leq 13$)	$y = 2.91 * x^{0.49}$ ($13 \leq x \leq 30$)
LWS1	$y = 0.58 + 0.06x$ ($0 \leq x \leq 30$)	
LWS2	$y = 0.73 + 0.09x$ ($0 \leq x \leq 30$)	
LWS3	$y = 0.24 + 0.17x$ ($0 \leq x \leq 13$)	$y = -2.10 + 0.36x$ ($0 \leq x \leq 13$)

and LWS2 rust was considerably better than that of CWS, resulting in the low corrosion rate of these two LWS. The 10CCT rust layer of LWS3 had a thickness of 24.10 μm and a compact structure. As the experiment proceeded, the thickness of the rust layer on LWS3 significantly increased. Specifically, the thickness of 30CCT reached 85.13 μm. The rust layer gradually loosened and developed cracks, eventually rupturing at 30CCT. This caused a large amount of Cl^- penetrate the rust layer, resulting in an increased corrosion rate for LWS3 in the later stages of the experiment. Despite this, the rust layer of LWS3 still exhibited some protective properties and a lower corrosion rate compared to CWS. The addition of Al and Mn inhibited the growth of the rust layer and enhanced its compactness in terms of thickness and crack number.

Figure 5 shows the cross-sectional distribution of elements in the rust layer of CWS and 30CCT of LWS.

The distribution of Fe clearly showed the thickness and shape of the rust layer of CWS. O was uniformly distributed in the rust layer of LWS. However, Fe concentration in the outer rust layer was significantly higher than that in the inner rust layer. Al was enriched in the inner rust layer of LWS, and the degree of enrichment increased with the increase in Mn content in the matrix. The distribution of Fe and Al can further clarify the interface between the inner and outer rust layers. The enrichment of Al in the inner layer had a significant impact on the morphology of the rust layer, which in turn affected the corrosion behavior of LWS. In addition, Mn was detected in the rust layer of LWS1 and LWS2, indicating that Mn was involved in the corrosion process of LWS. Figure 6 shows the Cl element distribution of rust layers in 30CCT. The point analysis was selected to accurately determine the distribution of Cl element. The locations of the point analysis are displayed in Fig. 4c, f, i and l. The results showed that the Cl concentration in the inner rust layer of CWS was slightly lower than that in the outer rust layer. Despite the thickness of the rust layer on CWS, its ability to block Cl^- was limited. In contrast, the rust layer on LWS1 and LWS2 was highly effective in preventing the penetration of Cl^-. The Cl concentration in the inner rust layer of LWS1 and LWS2 is much lower than
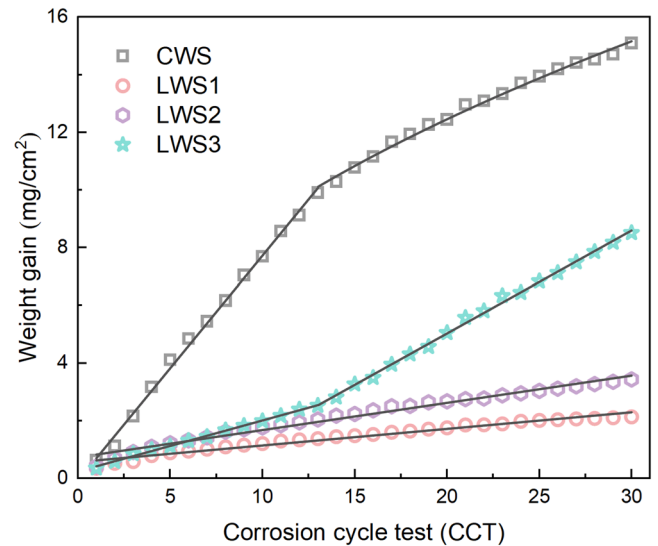
that in CWS. Meanwhile, Al was enriched in the inner rust layer of LWS1 and LWS2. The Al-enriched layer significantly increased the repulsion of Cl^-, resulting in a reduced corrosion rate compared to CWS. Although an Al-enriched layer was also present in the inner rust layer of LWS3, the rupture of the rust layer weakened its ability to prevent the attack of Cl^-, leading to an increase in the corrosion rate of LWS3 in the later stage of corrosion.

Figure 7 displays the surface morphologies of the rust layer at 30CCT. There are numerous holes on the surface of CWS, which provide a pathway for the electrolyte to penetrate the rust layer. In contrast, the surface of LWS1 is compact and free of holes. However, there are cracks on the surface of LWS2 and LWS3. The number of cracks on the surface of the LWSs increases as the Mn concentration decreases. The corrosion morphology of rust removal steels at 30CCT was observed by SEM (Fig. 8). It can be found that these steels have the same corrosion pattern, which is a combination of uniform corrosion and non-uniform corrosion. The substrate of CWS is severely corroded and there are deep corrosion pit. In contrast, the substrate of LWS1 exhibits slight corrosion with some shallow corrosion pits. The number of corrosion pits in the LWS increased as the Mn concentration decreased. This suggests that the addition of Mn restrained non-uniform corrosion. The corrosion loss rate of the experimental steels at 30CCT was calculated. The corrosion loss rates for CWS, LWS1, LWS2, and LWS3 are 0.316, 0.043, 0.072, and 0.171 mg cm^{-3} CCT, respectively.

Phase composition

The phase composition of the rust layer was analyzed using XRD, as shown in Fig. 9a–d. The phase composition of the CWS rust layer was consistent and included α-FeOOH, β-FeOOH, γ-FeOOH, and γ-Fe_2O_3.

In addition to these phases, $FeAl_2O_4$ was present in the corrosion product of LWSs, while MnO_2 was found in LWS1 and LWS2. α-FeOOH, β-FeOOH, γ-FeOOH, and γ-Fe_2O_3 were the main phases in the marine
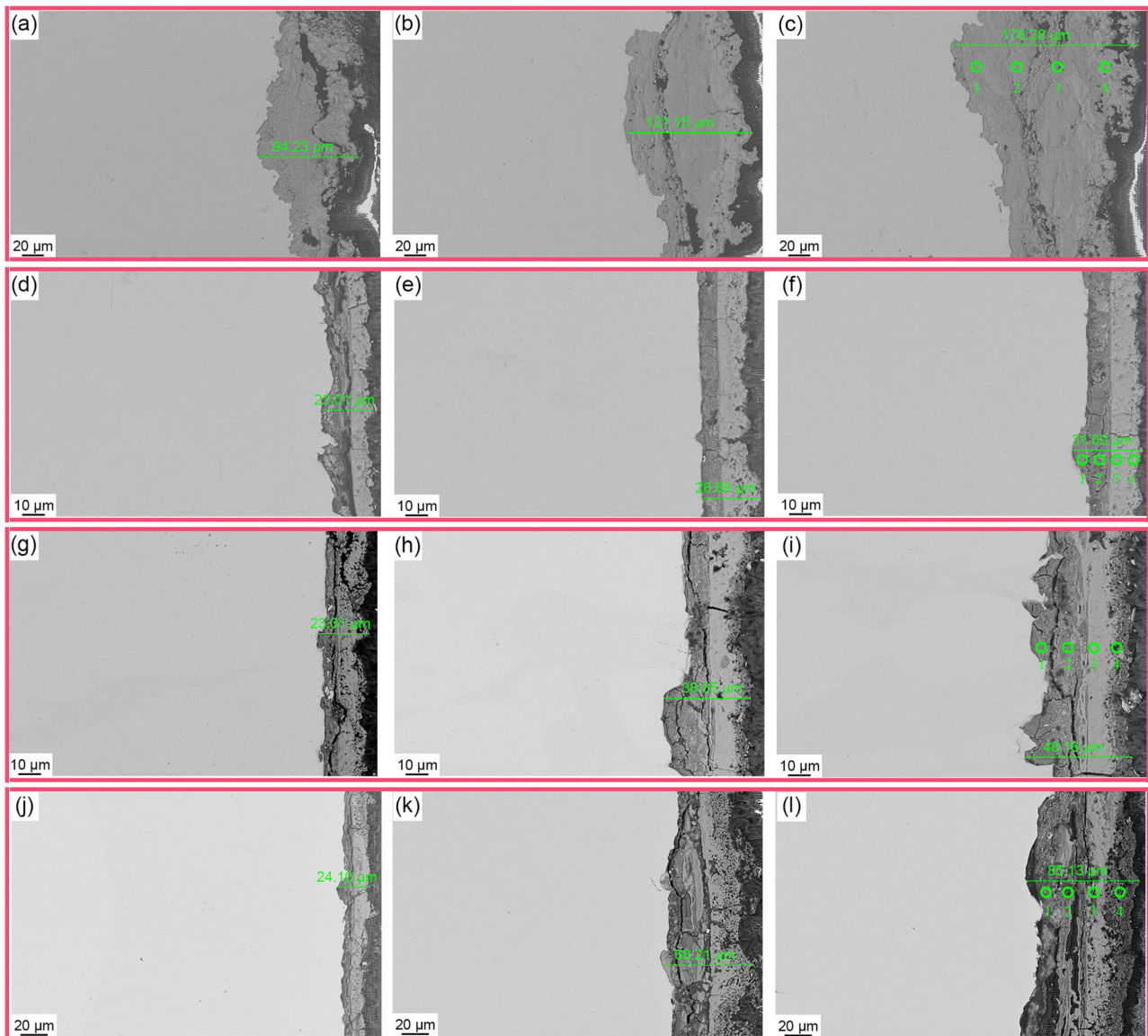
Fig. 4 | Cross-sectional morphologies of the rust layers. a–c CWS, **d–f** LWS1, **g–i** LWS2, and **j–l** LWS3 at **a, d, g, j** 10CCT, **b, e, h, k** 20CCT and **c, f, i, l** 30CCT, respectively.

atmosphere. However, the XRD peaks of rust showed variation in terms of intensity and width, indicating differences in the content of each phase in the rust layer. As the experiment proceeded, the peak intensities of α-FeOOH in all steels gradually increased. The compound with a relatively dense structure like α-FeOOH can retard the corrosion process. The XRD spectra indicate that the protectiveness of the rust layer increased with the passage of time. The α-FeOOH peak intensity of LWS increased more significantly than that of CWS. In the rust layer of LWS3, the intensity of the FeAl$_2$O$_4$ peak was weak and there was no MnO$_2$ peak. With the passage of time, the peak intensities of FeAl$_2$O$_4$ and MnO$_2$ in LWS1 and LWS2 intensified. The peaks of FeAl$_2$O$_4$ and MnO$_2$ in LWS1 were more intense than those in LWS2.

As shown in Fig. 10a–d, the XRD profiles were analyzed semi-quantitatively to express the ratio of different phases in the corrosion product. Numerous studies have concluded that α-FeOOH is the stable phase in the rust layer and has a superior ability to block corrosive ions than β-FeOOH, γ-FeOOH, and γ-Fe$_2$O$_3$[15,16]. α/γ* is considered a key index of the protectiveness of the rust layer, where α is the content of α-FeOOH and γ* is the total content of β-FeOOH, γ-FeOOH, and γ-Fe$_2$O$_3$[17–19]. As α/γ* increases, the protective properties of the rust layer improve. The α/γ* of CWS increased with time, reaching 44.56% at 30CCT. The results of α/γ*

showed that the corrosion resistance of CWS gradually improved. The α/γ* of LWS increased with the increase in CCT, ultimately achieving a superior protective ability. At 30CCT, LWS3 had a very high α/γ* value of 69.60%. The α/γ* and FeAl$_2$O$_4$ content increased simultaneously, with FeAl$_2$O$_4$ likely facilitating the conversion of α-FeOOH. The rust layer became more protective, and the conversion of γ-FeOOH to α-FeOOH became increasingly obvious with time. The content of MnO$_2$ and FeAl$_2$O$_4$ in the rust layer increased with the increase in Mn concentration. However, at 30CCT, the α/γ* of LWS1 and LWS2 decreased to 51.01% and 54.65%, respectively. The α/γ* of the rust layer decreased as the Mn concentration increased. This relationship indicated that the addition of Mn altered the contents of MnO$_2$ and FeAl$_2$O$_4$ in the rust layer and inhibited the conversion of α-FeOOH. The effect became more apparent with longer exposure times. In addition, the full width at half maximum (FWHM) of α-FeOOH(111), β-FeOOH(110), γ-FeOOH(200), and γ-Fe$_2$O$_3$ (311) were counted (Fig. 10e–h). The peaks of LWSs were found to be broader than those of CWS, indicating that the rust layer of LWSs is composed of finer grains according to Scherrer's equation. The increase in Mn concentration further broadens the peaks, suggesting that the synergistic effect of Al and Mn accelerates the nucleation process of the rust layer and retards its growth process.
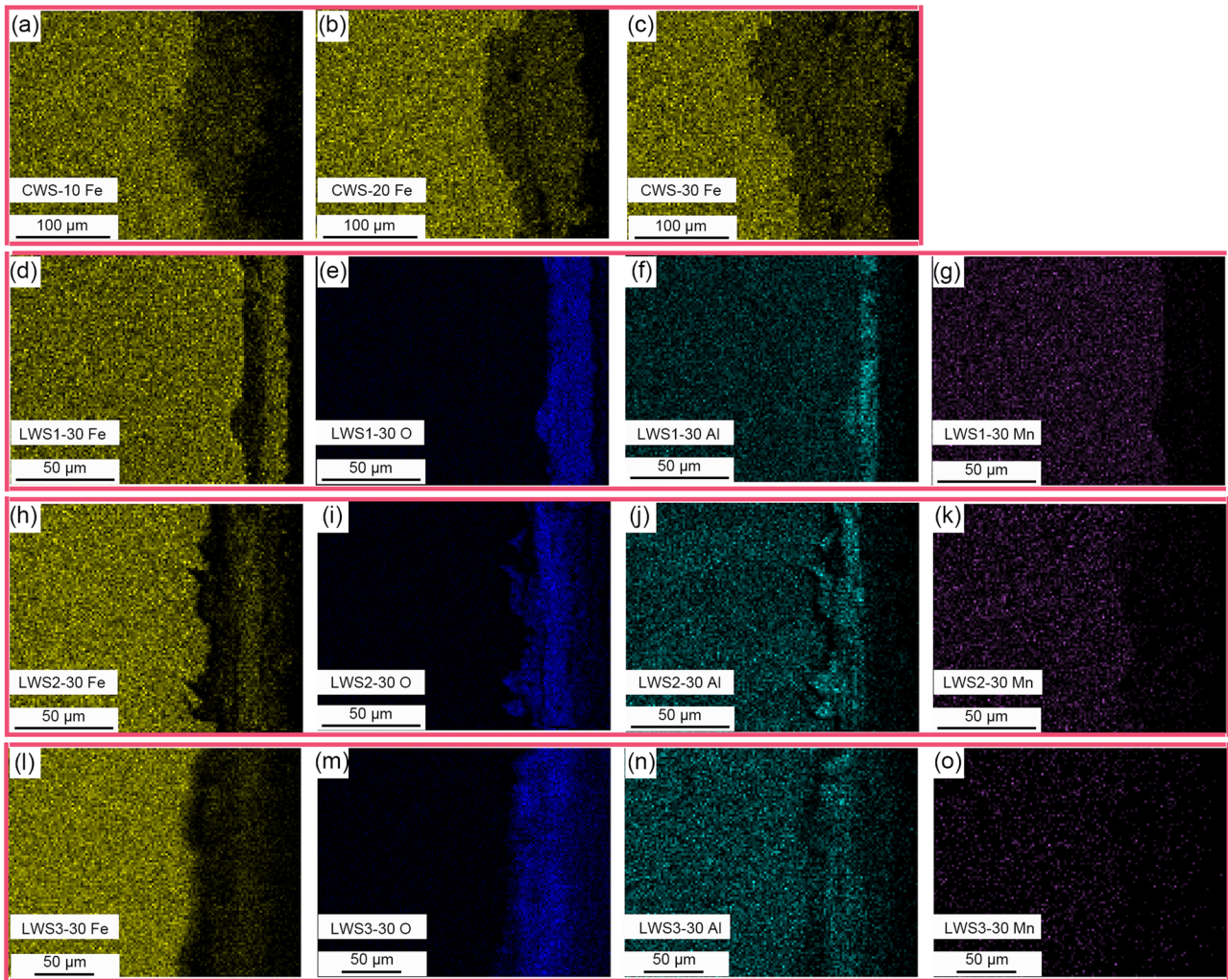
Fig. 5 | Element distribution of the rust layers. **a**–**c** CWS; element distribution of rust layer on the **d**–**g** LWS1, **h**–**k** LWS2, and **l**–**o** LWS3 in the 30CCT, respectively.
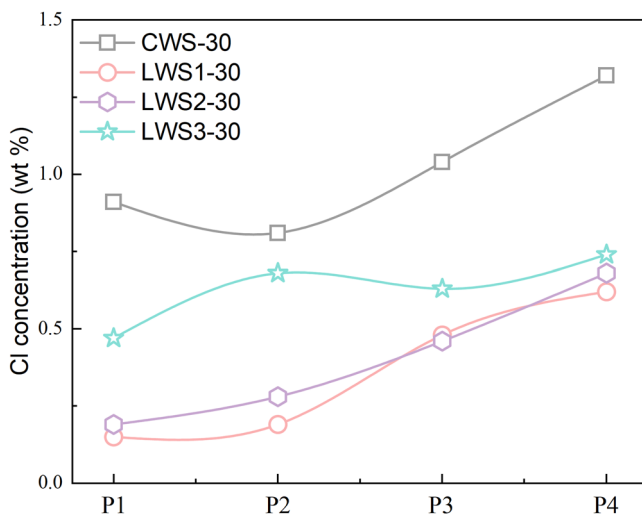
Fig. 6 | Cl element distribution of the rust layer at 30CCT.

The rust layer of weathering steel may contain an amorphous phase that cannot be accurately identified by XRD when it is mixed with the crystal phases[20,21]. In addition, the phase distribution in the inner and outer rust layers cannot be obtained by XRD. Therefore, the phase composition and distribution in the rust layer must be determined using Raman spectrometer. Figure 11a–d shows the Raman spectrometer results obtained with the cross-sections of CWS and LWS. Figure 11a illustrates that the phase components of the inner rust layer of CWS were mainly α-FeOOH and γ-FeOOH. In addition, small amounts of β-FeOOH and γ-Fe$_2$O$_3$ were detected. The main components of the outer rust layer of CWS were γ-FeOOH, α-FeOOH, and γ-Fe$_2$O$_3$, accompanied by a small amount of β-FeOOH. The inner rust layer had a higher α-FeOOH content and was denser and more protective than the outer rust layer. Figure 11b shows that the phase compositions of the inner rust layer of LWS1 differed significantly from those of CWS and consisted of a large amount of α-FeOOH. γ-FeOOH was also detected. Similar to those of CWS, the composition phases of the outer rust layer of LWS1 were also composed of γ-FeOOH, α-FeOOH, and γ-Fe$_2$O$_3$, as well as a small amount of β-FeOOH. The α-FeOOH signal was notably stronger in the inner rust layer of LWS1 compared to CWS. The addition of Al increased the α-FeOOH content of the inner rust layer. The phase composition and distribution of the rust layer of the other LWS (Fig. 11c, d) were similar to those of LWS1. However, the increase in Mn content weakened the intensity of the α-FeOOH peaks. This is consistent with the XRD results, which showed that the addition of Mn suppressed the conversion of α-FeOOH. XPS analysis was performed on the 30CCT rust layer of LWS to provide further clarification on the existing state of elements in the rust layer. Figure 11e shows that the XPS spectra of Al 2p in the rust layer can be divided into FeAl$_2$O$_4$ and Al$_2$O$_3$. The XPS spectra of Al were analyzed semi-quantitatively and the results are shown in Fig. 11f. The alterations in the relative contents of FeAl$_2$O$_4$ and Al$_2$O$_3$ suggested a possible conversion
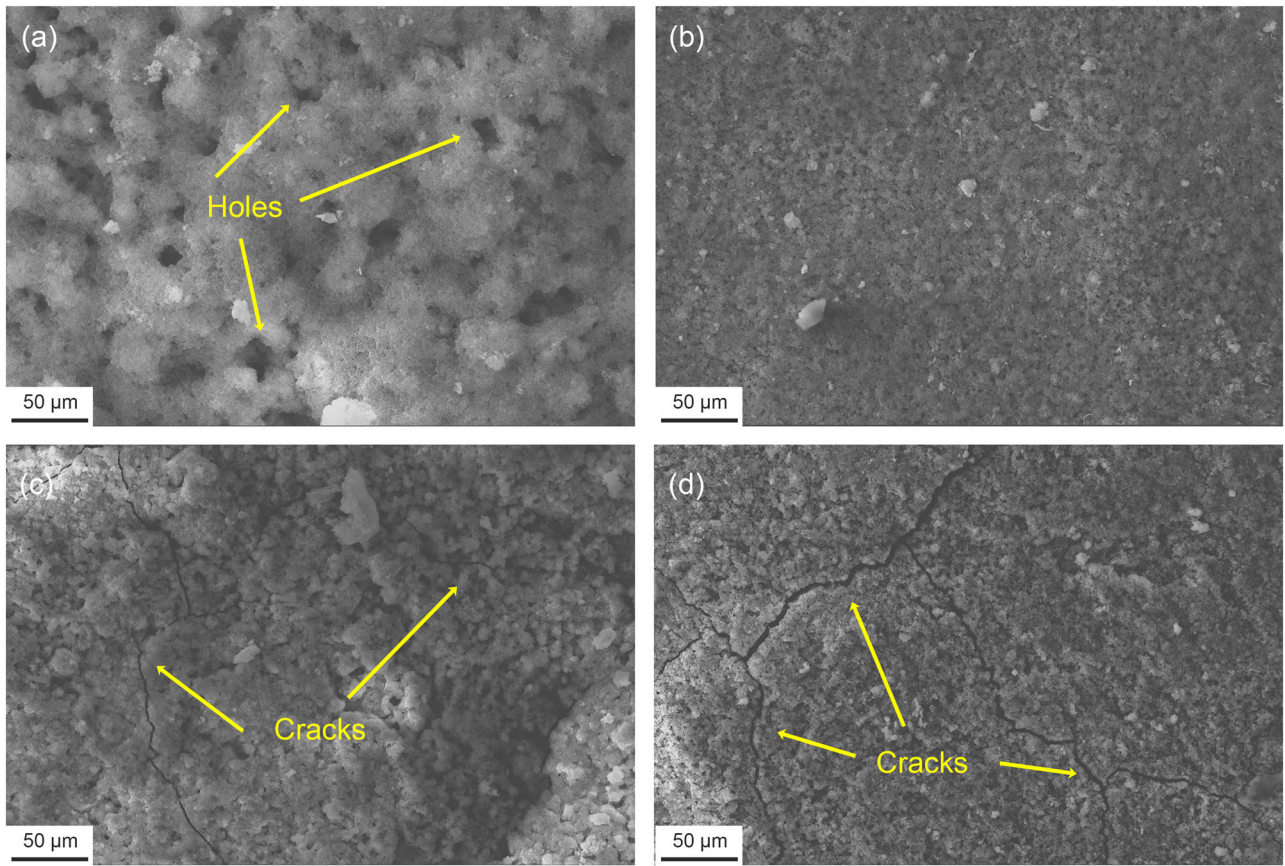
Fig. 7 | Surface morphologies of rust layer at 30CCT. a CWS, **b** LWS1, **c** LWS2, and **d** LWS3.
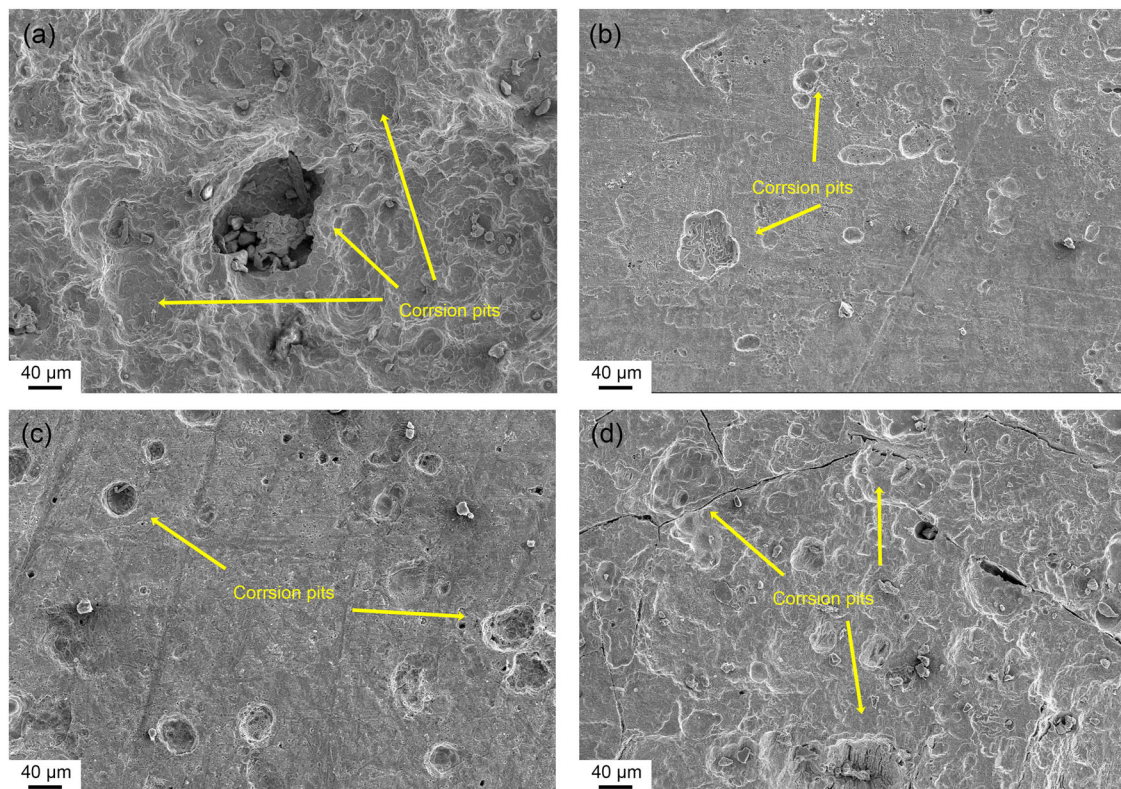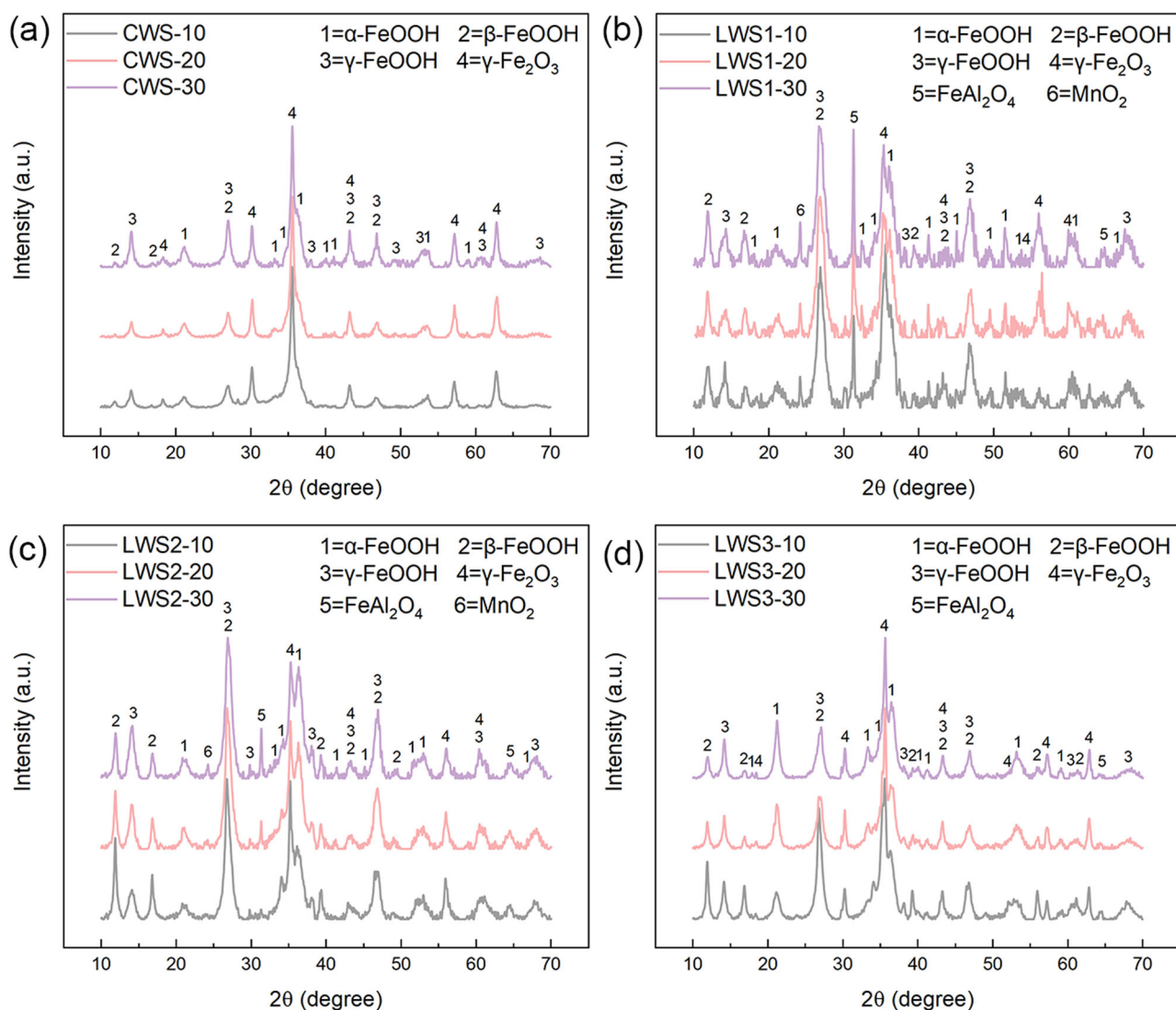

Fig. 8 | Corrosion morphology of rust removal steels at 30CCT. a CWS, **b** LWS1, **c** LWS2, and **d** LWS3.

Fig. 9 | XRD profile of rust layer. a CWS, **b** LWS1, **c** LWS2, and **d** LWS3.

relationship between the two, i.e., the conversion of Al_2O_3 to $FeAl_2O_4$, which is facilitated by the addition of Mn. The combined XRD and XPS results indicated that the formation of $FeAl_2O_4$ promoted the conversion from γ-FeOOH to α-FeOOH. Mn was detected in the rust layer as MnO and MnO_2 (Fig. 11g).

The 30CCT sample of LWS1 was tested using TEM to further analyze the inner rust layer of LWS. The sample selection locations are presented in Fig. 12a. The inner rust layer was composed of fine nanoparticles with a size of ~10 nm, as shown in Fig. 12b. The SAED pattern indicated that these grains contained α-FeOOH, β-FeOOH, γ-FeOOH, γ-Fe_2O_3, and $FeAl_2O_4$ (Fig. 12c). $FeAl_2O_4$ had a lattice spacing of 0.287 nm, which corresponded to the (220) plane (Fig. 12d). Elemental Fe, O, Al, and Mn were uniformly distributed in the inner rust layer and were all involved in the formation and growth of the rust layer. The enrichment of Al and Mn in the inner rust layer promoted the generation of $FeAl_2O_4$ and increased the protectiveness of the inner rust layer. Figure 12j–l shows that Al and Mn were enriched in the inner rust layer whereas Cl was blocked outside the inner rust layer. The enrichment of Al in the inner rust layer prevented contact between Cl^- and the matrix by blocking the Cl^-.

**Electrochemical properties**

Figure 13 shows potentiodynamic polarization curves and corresponding corrosion parameters for weathering steels. The main controlling factors of the cathodic process are the reduction of the rust layer and O, whereas the anodic process is mainly the dissolution of the matrix. The downward movement of the potentiodynamic polarization curves indicates an inhibition of the electrochemical reaction. The curves of CWS at different CCTs showed active dissolution. In contrast, all anodic branches of LWS exhibited pseudo-passivation, suggesting that the rust layer of LWS was more capable of blocking corrosive ions. The corrosion parameters (E_{corr} and i_{corr}) were using the Tafel extrapolation method from the cathodic curve, which was done because the anodic does not follow the Tafel empirical law due to the passivation reaction[22]. The E_{corr} and i_{corr} express the thermodynamics and kinetics of corrosion, respectively, with high E_{corr} and low i_{corr} indicating lower corrosion tendencies and corrosion rate[23]. Throughout the corrosion process, the thickness and corrosion resistance of the rust layer increase, leading to a reduction in corrosion tendency and rate. The corrosion potential and corrosion current density of LWS1 and LWS2 were superior to those of CWS, showing better corrosion resistance. However, the corrosion performance of LWS3 significantly deteriorated in the later stage of the experiment due to the rupture of the rust layer.

The EIS test was performed to further understand the effect of the rust layer on the corrosion resistance performance of the experimental steels. EIS tests were performed on the rust layer in a NaCl solution with the same concentration as the corrosion solution to evaluate the protective capacity of the rust layer. Figure 14 shows the EIS curves of CWS and LWSs. Both the
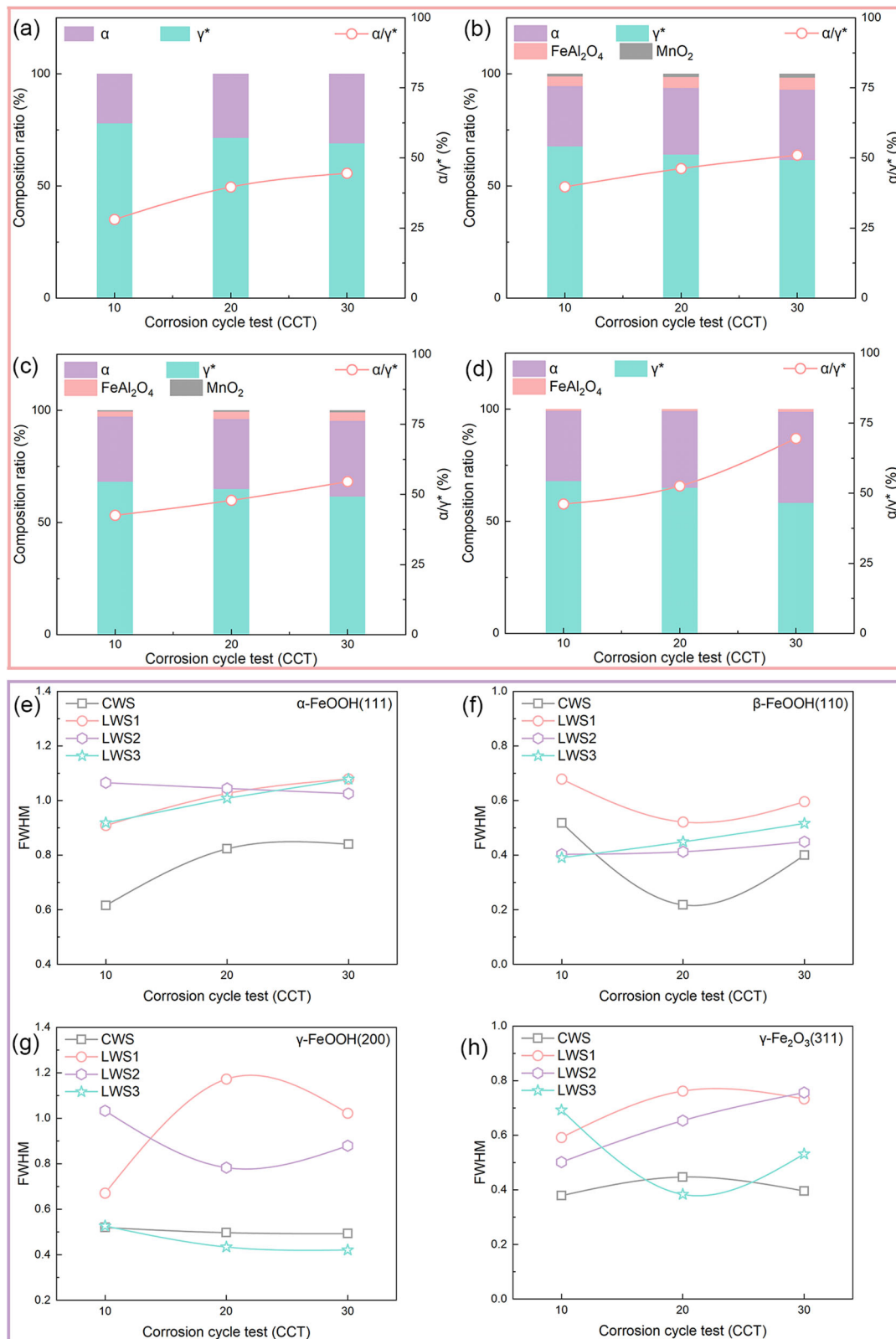
Fig. 10 | XRD parameters. Phase proportion and α/γ* of rust layer on **a** CWS, **b** LWS1, **c** LWS2, and **d** LWS3; FWHM results of **e** α-FeOOH(111), **f** β-FeOOH(110), **g** γ-FeOOH and **h** γ-Fe₂O₃(311).

semicircle diameter in the Nyquist plots and $|Z|_{0.01HZ}$ in the Bode-impedance plot increased gradually, indicating that the protective effect of all steels increased with the increase in CCT. Given the poor initial compactness of the rust layer, there are many cracks and holes, which allow Cl⁻ to easily reach the matrix through the rust layer and accelerated corrosion.

The related EIS parameters continued to increase due to the densification of the rust layer on weathering steels, indicating good stability and protection. Throughout the experiment, the semicircle diameter of the Nyquist plot and $|Z|_{0.01HZ}$ of the Bode-impedance plot of LWS were higher than those of CWS and followed the order of LWS1 > LWS2 > LWS3. The angle diagram

Fig. 11 | Results of Raman spectra and XPS. Raman spectra of 30CCT measured on **a** CWS, **b** LWS1, **c** LWS2, and **d** LWS3 (G: α-FeOOH, A: β-FeOOH, L: γ-FeOOH, M: γ-Fe$_2$O$_3$); XPS spectra of **e** Al in rust layer of 30CCT of LWS; **f** ratio of Al compound of LWS; XPS spectra of **g** Mn in rust layer of 30CCT of LWS1.
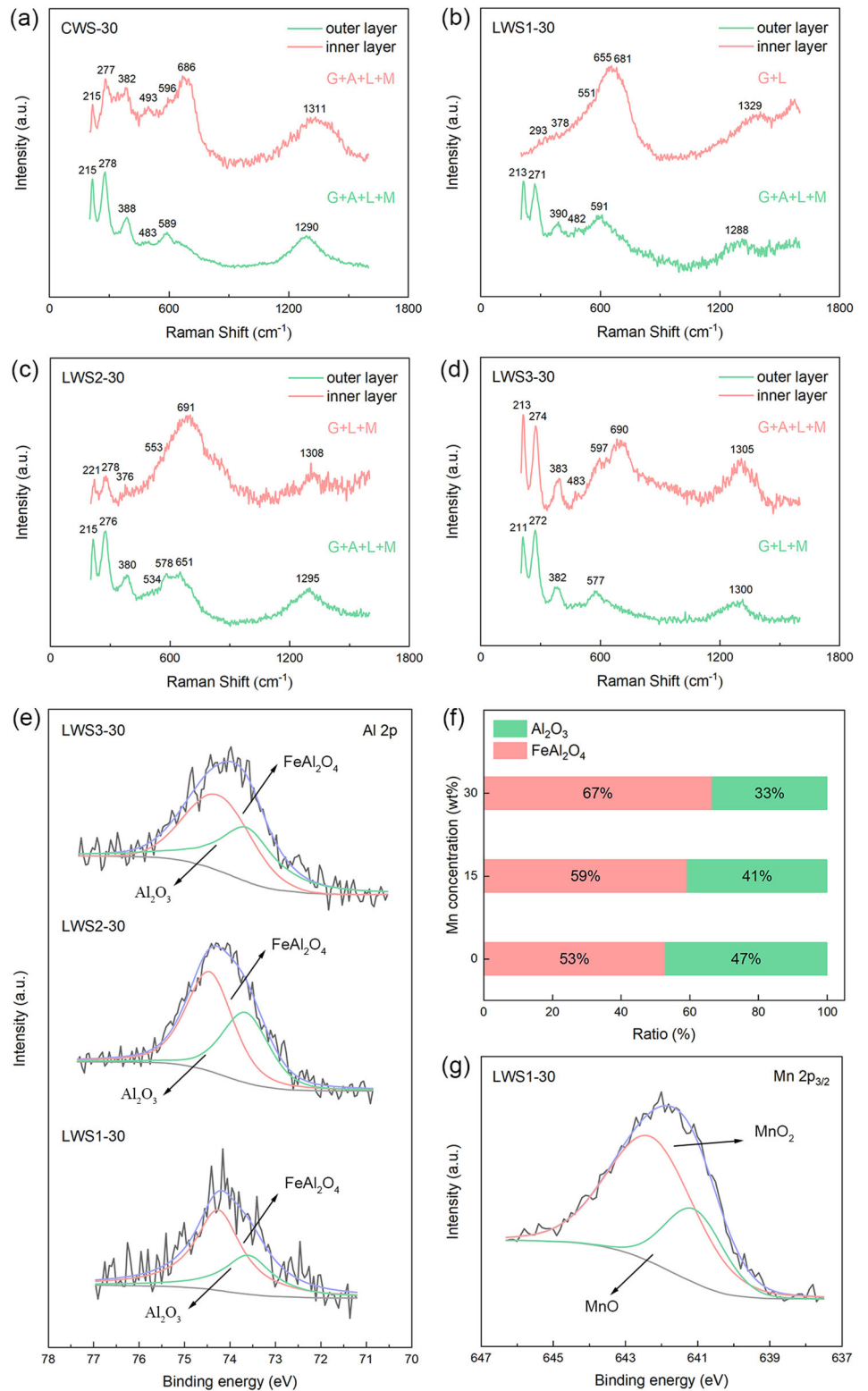
(Fig. 14c, f, i, l) indicates that the resistance of the rust layer against the permeation of the corrosion solution gradually strengthened as the peaks of the phase angle of experimental steel gradually increased. The peaks of the phase angle in all curves were less than 90°. Generally speaking, this behavior can be interpreted as a deviation from the ideal capacitor characteristics resulting from the inhomogeneities in the electrodes, porosity, mass transport, and relaxation effects[24,25]. The peaks of the phase angle decreased in the following order: LWS1 > LWS2 > LWS3 > CWS, and the

compactness of the rust layer followed the same trend. Obviously, the trend of the protective properties of the rust layer was the same.

The EIS data of steels is simulated by the equivalent electrical circuit in Fig. 15. R_s is the resistance of the solution, CPE$_{rust}$ is the capacitance of the rust layer, R_{rust} is the resistance of the rust layer, CPE$_{dl}$ is the capacitance of the double layer, R_{ct} is the charge transfer resistance. Table 3 shows the fitting results of the rust layer. n is the index of CPE, which is the ideal capacitance when n is 1. Obviously, the n_{rust} and R_{ct} of the experimental steel increased
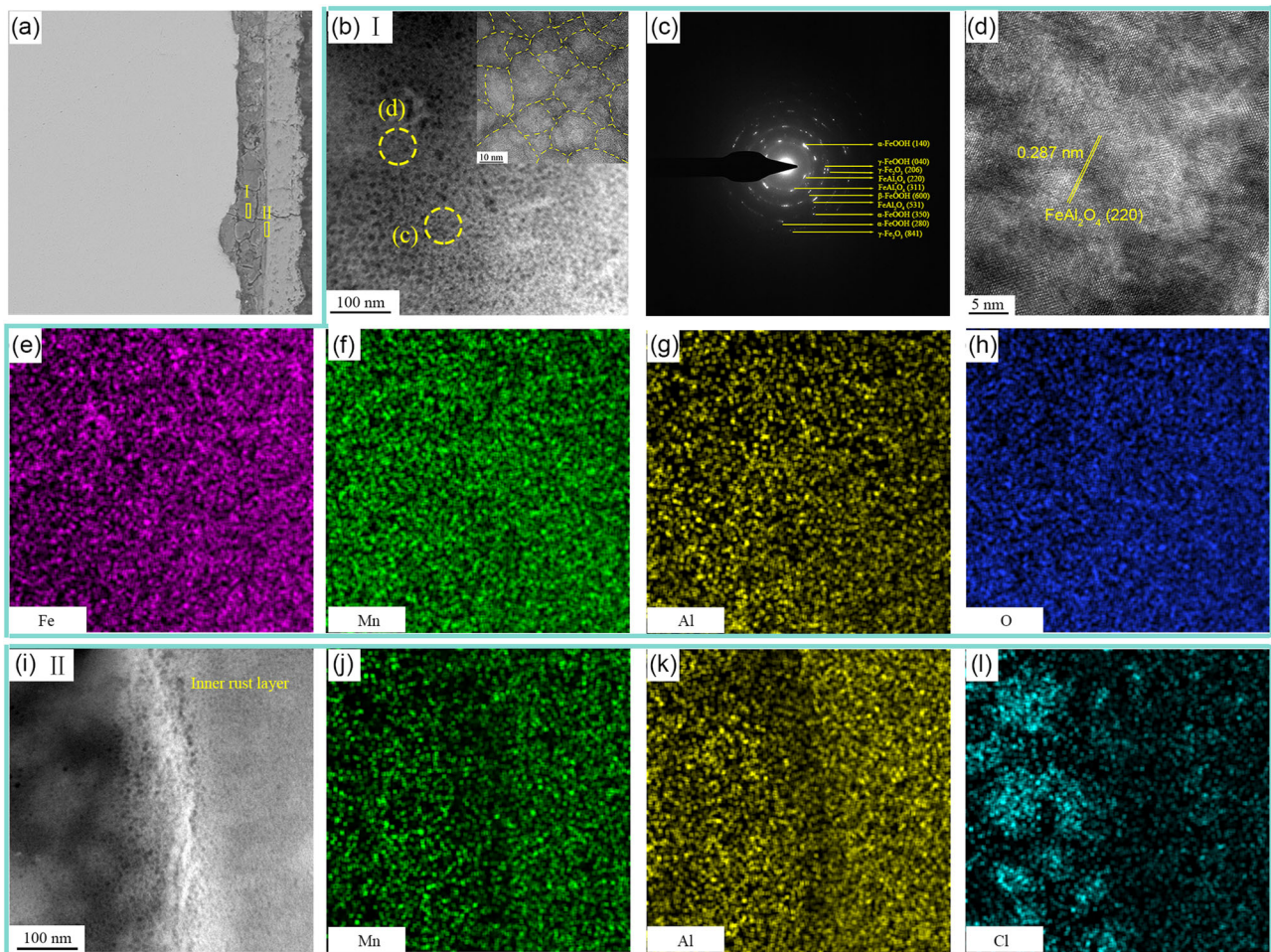
Fig. 12 | TEM results of LWS1. a The TEM samples of I and II for LWS1; **b** TEM image of I; **c** SAED pattern of (**b**); **d** HRTEM image of $FeAl_2O_4$ in (**b**); **e–h** EDS mapping of I; **i–l** TEM image and EDS mapping of II.

with time. Corrosion resistance decreased on the order of LWS1 > LWS2 > LWS3 > CWS. This trend became more obvious with time, especially with the increase in n_{rust} and R_{ct}. This result indicated that rust layers with high $FeAl_2O_4$ contents are more compact and resistant to the transport of Cl^- and O_2. The n_{rust} and R_{ct} of LWS3 decreased at 30CCT, and the conclusions of EIS were consistent with the variation in corrosion rate.

Discussion

LWS is more suitable for use in the marine atmosphere than CWS due to its excellent corrosion resistance. The rust layer that formed on LWS is superior for the following reasons: The rust layer of LWS showed a better physical structure. The structure of the rust layer was uniform and compact, without large cracks and holes. Therefore, the rust layer effectively blocked Cl^- and O_2 from coming into contact with the matrix. In addition, it exhibited durable compactness in the marine atmosphere, and the compactness increased with time, a property that is important for corrosion retardation.
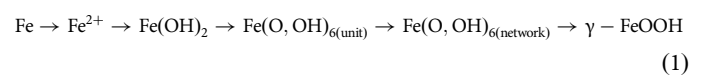
The rust layer of LWS had a superior phase composition and distribution. Although the main phases of the rust layer on LWS were the same as those on CWS, the rust on LWS had a higher α-FeOOH content and contained $FeAl_2O_4$. $FeAl_2O_4$ is considered to possess an AB_2O_4 spinel crystal structure where cation A has two positive unit charges and cation B has three positive unit charges. $FeAl_2O_4$ is a mixed oxide normal spinel in which Fe^{2+} occupies one-eighth of the tetrahedral sites and Al^{3+} occupies half of the octahedral sites. The contents of α-FeOOH and $FeAl_2O_4$ increased with time. In addition, α-FeOOH and $FeAl_2O_4$ were more present in the inner rust layer than in the outer rust layer, and their increase significantly optimized the phase composition and distribution of the rust

layer, thus improving its protective effect. A large number of Cl^- were effectively blocked by the inner rust layer, and the acceleration of corrosion by Cl^- was mitigated because Cl^- could not come into direct contact with the steel matrix, and the localized corrosion at the rust/steel interface decelerated because of the weakened localized acidification[26,27].

The rust layer of LWS exhibited better electrochemical properties. The electrochemical analysis showed that the rust layer of LWS resulted in a high capacitive reactance arc in 0.3% NaCl solution, and the radius continued to enlarge with the increase in corrosion time, indicating that the rust layer provided great resistance against corrosion. The R_{ct} and n_{rust} values obtained from the EIS curve illustrated that the rust layer participated in blocking electron transport and material transfer, and the blocking effect intensified.

In summary, owing to its superior physical structure, phase composition and distribution, and electrochemical properties, the rust layer of LWS provided better protection, thus effectively reducing the corrosion rate in the marine atmosphere.

Previous studies showed that the corrosion of steel in the marine atmosphere is mainly affected by oxygen and Cl^- in the electrolyte on the steel surface. Fe dissolves and generates Fe hydroxides and oxides, and the relevant reactions in corrosion are as follows:

$$Fe \rightarrow Fe^{2+} \rightarrow Fe(OH)_2 \rightarrow Fe(O, OH)_{6(unit)} \rightarrow Fe(O, OH)_{6(network)} \rightarrow \gamma - FeOOH$$

$$(1)$$

γ-FeOOH is unstable and can convert into α-FeOOH, β-FeOOH, or γ-Fe_2O_3. The atomic structures of α-FeOOH, β-FeOOH, and γ-FeOOH consist of $Fe(O, OH)_6$ octahedra, with varying stacking sequences of $Fe(O,$
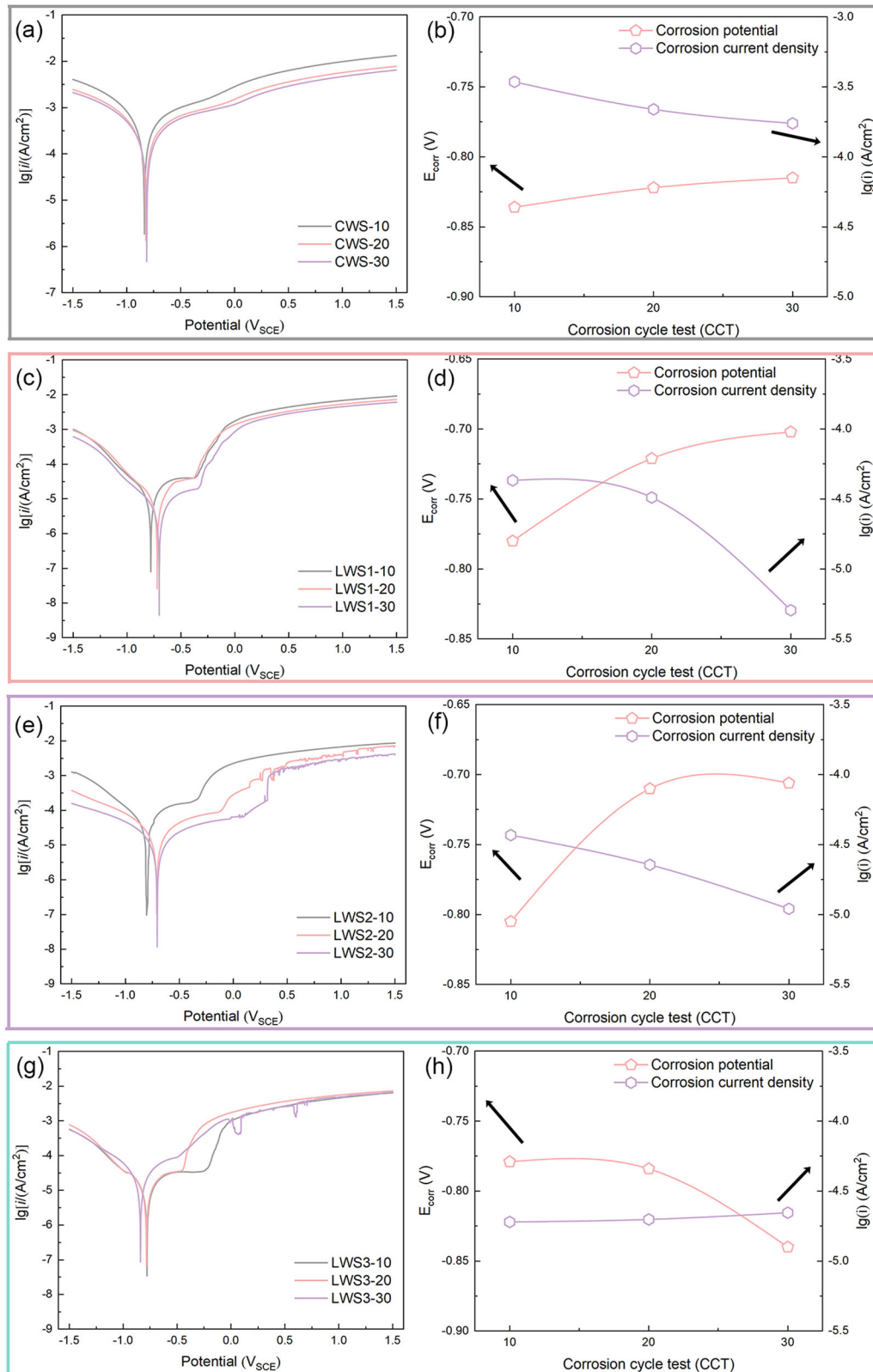
Fig. 13 | Potentiodynamic polarization curves and corresponding corrosion parameters. a, b CWS, c, d LWS1, e, f LWS2 and g, h LWS3.

$OH)_6$. The corrosion resistance of weathering steel is closely related to the chemical and physical properties of the rust layer[28,29]. The rust layer of CWS and LWS had the same main compositional phases and consisted of α-FeOOH, γ-FeOOH, and γ-Fe$_2$O$_3$. The stability of the network structure of $Fe(O, OH)_6$ decreased because of the high Cl$^-$ concentration, which hinders

the conversion of γ-FeOOH into the more stable α-FeOOH but prefers to dehydrate to form γ-Fe$_2$O$_3$[30,31].

The corrosion of carbon steel proceeded rapidly because of the high corrosion rate. The growth rate of the rust layer was higher than the nucleation rate, the rust layer consisted of relatively large grains
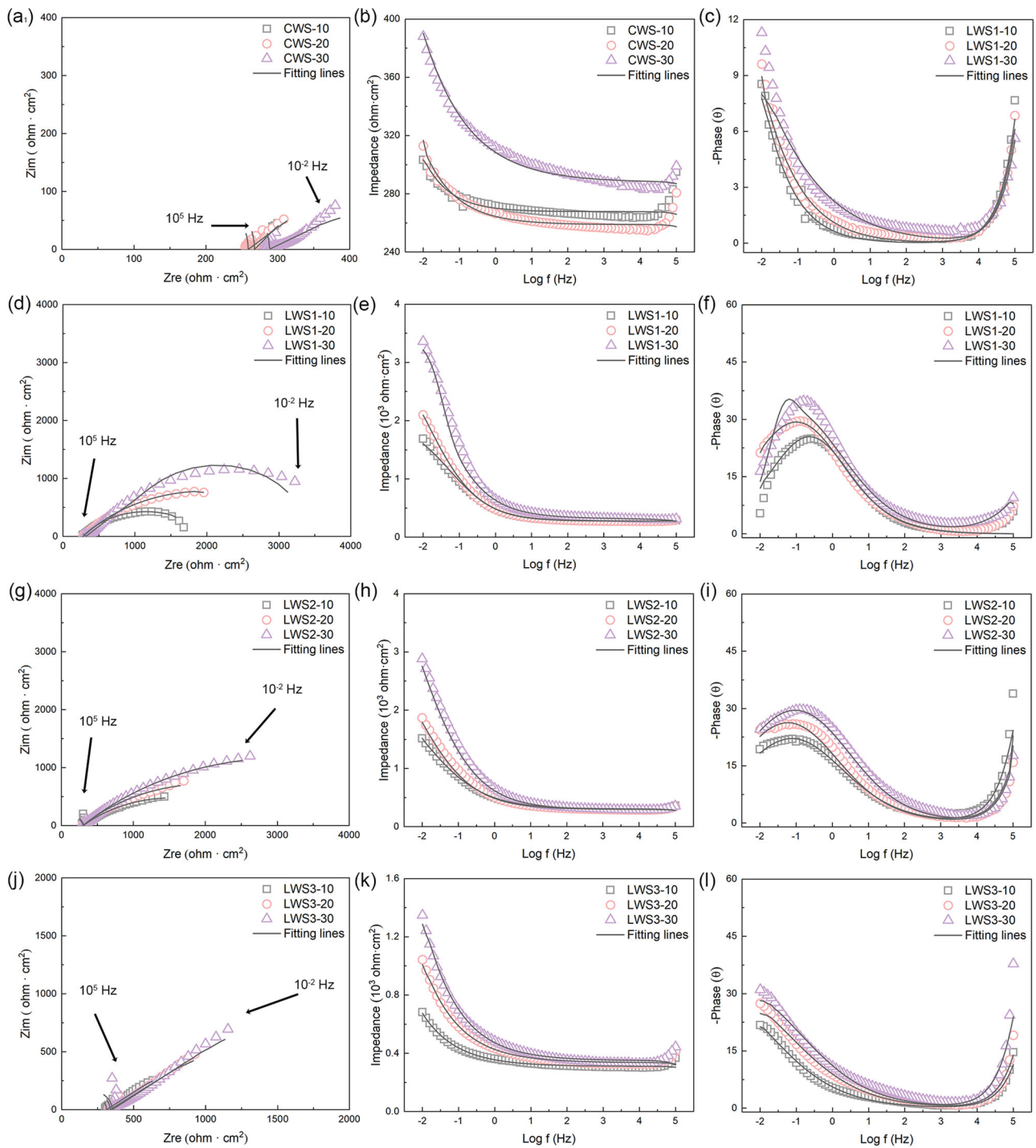
Fig. 14 | The EIS curves. a–c CWS, **d–f** LWS1, **g–i** LWS2, and **j–l** LWS3.

containing voids and defects[32], and Cl⁻ and oxygen easily penetrated the grain boundaries[33]. The main products of carbon steel were α-FeOOH and γ-FeOOH. When the rust layer becomes wet and corrosion occurs in a high-salt atmosphere, the pH of the wet rust layer decreases because of the hydrolysis of the metal cations. Subsequently, the hydroxyl (-OH) on the surface of the rust layer transforms into $-OH^+_2$, leading to the formation of positive charges on the rust, and Cl⁻ easily approaches the rust/steel interface[34]. The main alloying elements in weathering steel are also involved in the formation of the rust layer and influence the morphology and performance of the rust layer. At the early stage of corrosion, Fe_2NiO_4 and CuO are precipitated, thus providing nucleation sites for the $Fe(O, OH)_6$ network, and the nucleation rate is higher than the

growth rate, resulting in the formation of rust consisting of fine and compact grains[34].

Al is an important element in LWS, Al reacts with O_2 to form Al_2O_3. Some part of Al_2O_3 is also involved in the formation of $FeAl_2O_4$, and the relevant chemical equations are as follows:

$$4Al + 3O_2 \rightarrow 2Al_2O_3 \tag{2}$$

$$Fe(OH)_2 + Al_2O_3 \rightarrow FeAl_2O_4 + H_2O \tag{3}$$
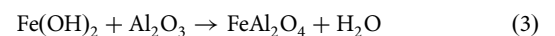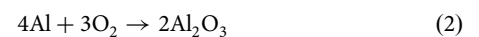
Al is mainly present in the inner rust layer in the form of $FeAl_2O_4$. EDS and XRD results confirmed that the involvement of Al resulted in the

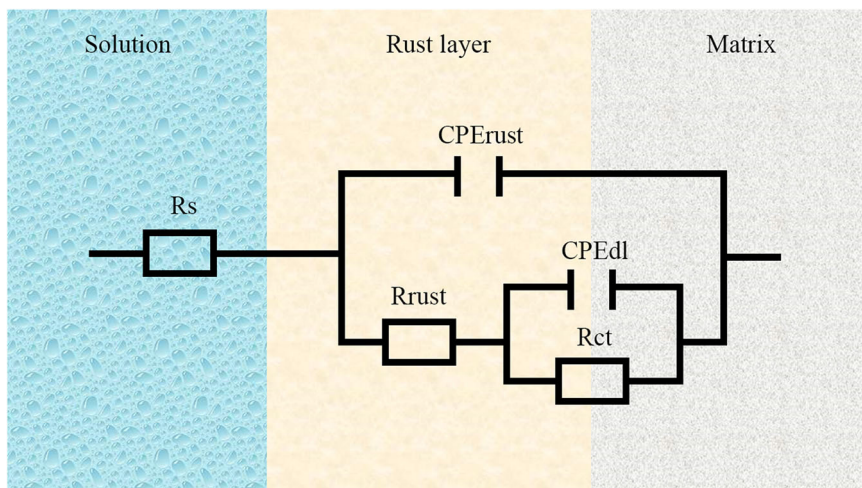**Fig. 15 |** Equivalent electrical circuit for the EIS data.

Table 3 | Fitted parameters of the EIS curves of CWS and LWS by equivalent electrical circuit

Steel	R_s ($\Omega \cdot cm^2$)	CPE_{rust} ($\Omega^{-1} \cdot cm^{-2} \cdot S^n$)	n_{rust}	R_{rust} ($\Omega \cdot cm^2$)	CPE_{dl} ($\Omega^{-1} \cdot cm^{-2} \cdot S^n$)	n_{dl}	R_{ct} ($\Omega \cdot cm^2$)
CWS-10	268.4	9.519 E-2	0.3992	31.27	1.491 E-2	0.5481	117.3
CWS-20	255.5	3.348 E-2	0.4554	43.80	4.971 E-2	0.5585	218.3
CWS-30	283.5	7.639 E-3	0.4565	65.22	2.864 E-2	0.5536	336.9
LWS1-10	276.7	3.913 E-3	0.6041	136.8	1.062 E-3	0.6252	1146
LWS1-20	273.3	1.271 E-3	0.6292	347.9	1.630 E-4	0.6705	2766
LWS1-30	311.8	2.211 E-4	0.6356	453.9	5.952 E-4	0.6637	4083
LWS2-10	202.8	6.692 E-3	0.5904	147.4	1.138 E-3	0.5336	1273
LWS2-20	287.8	4.017 E-3	0.6415	357.5	2.35 E-3	0.6073	2837
LWS2-30	282.6	8.354 E-4	0.6546	398.3	1.06 E-4	0.6447	3946
LWS3-10	300.4	4.559 E-3	0.6108	158.5	5.489 E-3	0.5797	1128
LWS3-20	329.1	2.926 E-3	0.6395	376.6	4.129 E-3	0.6071	2580
LWS3-30	322.4	2.818 E-3	0.5446	289.9	4.304 E-3	0.5775	1456

formation of a better rust layer. In the marine atmosphere, the Al content in the rust layer gradually increased with time. Specifically, the appearance of $FeAl_2O_4$ and the increase of $FeAl_2O_4$ in the rust layer were responsible for the increased protectiveness of the rust layer against corrosion.

The Fe-Al potential-pH diagram shows that $FeAl_2O_4$ existed stably, and this spinel oxide is understood to prevent corrosion[35]. The properties of the rust layer on LWS were significantly altered by the formation of $FeAl_2O_4$. Firstly, $FeAl_2O_4$ changed the morphology of the rust. Since alloying elements, such as Al can increase the number of reaction sites for rust evolution. The nucleation energy of $FeAl_2O_4$ differed from that of $Fe(O, OH)_6$, which may reduce the nucleation activation of the corrosion product. On the basis of their standard electrode potential, Al (-1.66 v) is more active than Fe (-0.44 v) in a corrosive medium. In the early stage of the corrosion process, the formation of $FeAl_2O_4$ provided nucleation sites for the $Fe(O, OH)_6$ network. The increase in reaction sites and the decrease in the nucleation activation of corrosion products will enhance nucleation. Given that $FeAl_2O_4$ and $Fe(O, OH)_6$ have different structures, $FeAl_2O_4$ influenced the evolution of $Fe(O, OH)_6$, thus distorting the $Fe(O, OH)_6$ network[33]. Eventually, rust consisting of fine, dense grains was formed. In the early stage of corrosion, LWS generated $FeAl_2O_4$, which was highly protective and resulted in a low corrosion rate. The generation of $FeAl_2O_4$ accelerated the formation of nanoscale α-FeOOH in the rust layer rather than the conversion of γ-FeOOH into β-FeOOH or γ-Fe_2O_3. As a result, the α/γ* of LWS increased as the experiment progressed. The increase in α-FeOOH and $FeAl_2O_4$ improved the stability and compactness of the rust layer. The rust

layer consists of fine grains is expected to retard the diffusion of Cl^- and O_2 along the grain boundaries. Therefore, the formation of a fine rust layer can reduce the corrosion reaction rate.

Secondly, $FeAl_2O_4$ changed the ion-exchanging properties of the rust layer. $FeAl_2O_4$ was stably present in the inner rust layer. The $Fe(O, OH)_6$ network in the inner rust layer contained a large amount of $FeAl_2O_4$. As a result of the spinel structure and the low oxidation-number averaged over metals, the grain boundaries or surfaces of the inner rust grains were more negative than those of grains containing only the FeOOH phase, and the grain boundaries or surfaces of the inner rust layer were also more negative than those of the outer rust layer[36,37]. This situation effectively inhibited the penetration of anions (especially Cl^-), thus preventing the accumulation of negative Cl^- in the rust grains, which prevented the pH from decreasing at the rust/ steel interface[38]. Therefore, it can be assumed that the increase in $FeAl_2O_4$ content significantly improves the electronegativity and anion selectivity of the rust layer, especially the inner rust layer.

The presence of $FeAl_2O_4$ improved the physicochemical properties of the rust layer, including the phase composition and distribution, and electrochemical properties. These improvements were always assured with prolonged exposure due to the continuous enrichment of $FeAl_2O_4$ in the inner rust layer. The schematic diagram of the corrosion mechanism is shown in Fig. 16.

The ΔG of Eqs. (2) and (3) are -3164.6 and -154.5 KJ mol^{-1}, respectively. The calculated values for both reactions suggest that the

Fig. 16 | Schematic diagram of the corrosion mechanism. a CWS and **b** LWS.
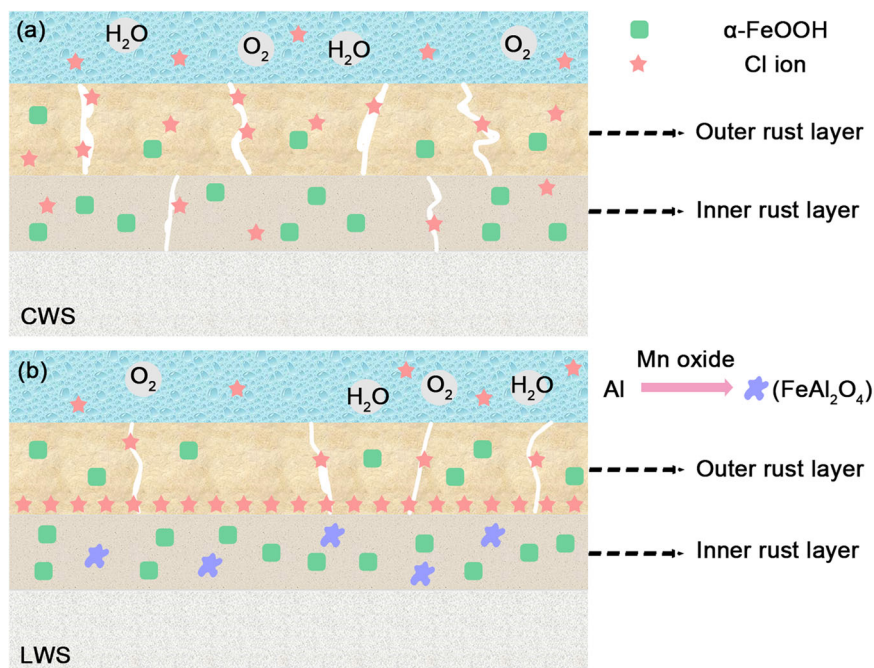
transformation from Al to $FeAl_2O_4$ can occur spontaneously. Numerous studies indicate that Mn oxides can serve as catalysts or modifiers to enhance the battery materials' performance[39,40]. The Mn oxide particles within the rust layer form a rigid framework that can serve as catalytically active sites, providing a fast electron and ions transportation path, reducing the energy barrier, and accelerating the reaction. The catalytic characteristic of Mn oxide, which is conducive to electronic transfer, promotes the transformation of Al to $FeAl_2O_4$. This becomes more pronounced with increasing Mn concentration. During corrosion, $FeAl_2O_4$ was enriched in the inner rust layer. This effect not only provided nucleation sites for nanoscale α-FeOOH but also filled the holes and cracks in the rust layer. This effect was conducive to the generation of a denser rust layer with improved protection. However, the increase in Mn content led to the preferential participation of γ-FeOOH in the cathodic reaction instead of its conversion to α-FeOOH[41]. The reduction in α-FeOOH content affected the compactness of the rust layer. However, the generation of $FeAl_2O_4$ may not only increase compactness; it may also reduce cracks and improve the protective effect of the rust layer.

The highest α/γ^* of the rust layer was observed for 30CCT in the LWS3 sample. However, the rust layer ruptures in the later stages of the experiment, leading to a significant increase in the corrosion rate. As the rust layer thickened, dry-wet cycles and phase transitions introduced stress into the rust layer, leading to increased cracking[42] (FeOOH is an ionic compound that determines the brittle nature of the rust layer. Even if the rust layer is dense, excessive stress will cause it to crack to release stress and accelerate the steel corrosion[43]). The crack of the rust layer prolongs the stagnation time of the solution and lowers the pH value within the crack due to the hydrolysis of the metal ions. The crack provides an ideal location to become a favorable anodic corrosion condition, promoting further corrosion reaction leading to greater acidification and stabilizing corrosion within the crack. Excessive cracking can cause the rust layer to rupture, resulting in a rapid increase in corrosion rate. The rust layer of LWS3 ruptured at 30CCT. The addition of Mn increased the content of $FeAl_2O_4$, enhanced the protective properties and anti-rupture ability of the LWS's rust layer. As a result, LWS1 and LWS2 exhibit high compactness and excellent corrosion resistance in the later stages of the experiment.

In the current CCT, the lightweight weathering steel showed better corrosion resistance and we are willing to further evaluate the corrosion resistance of lightweight weathering steel in the atmosphere through

weathering test. We hope to obtain more detailed experimental data to promote the development of weathering steel.

The rust layer formed on LWS in the marine atmosphere was systematically studied, and the following conclusions can be drawn:

The rust layer formed on LWS exhibits corrosion resistance and a low corrosion rate. The rust layer of LWS shows significant advantages over CWS in terms of physical structure, phase composition and distribution, and electrochemical properties.

The $FeAl_2O_4$ in the inner rust layer provided nucleation sites for $Fe(O, OH)_6$, which refines the grains and promotes α-FeOOH generation. The holes and cracks in the rust layer were filled with $FeAl_2O_4$ and the compactness of the rust layer was improved. Additionally, the enrichment of $FeAl_2O_4$ in the inner rust layer produced an electronegative effect that blocks Cl^-. This effect becomes more pronounced with time.

The addition of Mn promoted the formation of $FeAl_2O_4$ while inhibiting the conversion of α-FeOOH. As the Mn content increases, the rust layer of LWS tends to become compact and crack-free. The addition of Mn prevents rupture of the LWS's rust layer caused by stress release.

Methods
Alloy preparation
The chemical compositions of the weathering steels are listed in Table 4. For convenience, the conventional weathering steel is referred to as CWS, and the lightweight weathering steels with various Mn concentrations are referred to as LWS1, LWS2, and LWS3, respectively. CWS was a hot rolled steel plate manufactured by Angang Steel Company Limited. The LWS material was melted using a 50 Kg vacuum induction melting furnace under an Ar atmosphere. Steel molds were utilized for casting and air–cooled to room temperature after pouring. The ingots were forged at 1115 °C and air–cooled to room temperature. Subsequently, they were heated to 1050 °C and repeatedly rolled 6 times to obtain a steel plate with a thickness of 5 mm (total reduction: 75%).

Microstructure observation
The microstructure of the experimental steels was observed by optical microscope (OM; Zeiss Axiovert 200 MAT). The OM samples were sanded with 4000# SiC sandpaper and subsequently polished to a mirror finish. Afterward, they were etched with 15% Nital. The uniaxial tensile tests were

Table 4 | Chemical compositions of CWS and LWS (wt%)

Steel	Mn	Al	C	Si	Cu	Ni	P	S	Cr	Fe
CWS	0.37	0.06	0.089	0.43	0.36	0.29	0.123	0.011	0.66	Bal.
LWS1	29.93	5.08	0.097	0.31	0.39	0.28	0.015	0.005	0.44	Bal.
LWS2	15.04	5.02	0.102	0.33	0.38	0.31	0.016	0.006	0.42	Bal.
LWS3	0.02	5.10	0.004	0.30	0.41	0.30	0.015	0.005	0.45	Bal.

carried out at room temperature using a universal testing machine (Instron 5982). Each condition was repeated thrice to ensure reproducibility.

Corrosion cycle test

All steels were processed into samples with dimensions of $15 \, mm \times 15 \, mm \times 4 \, mm$ for the corrosion cycle test (CCT), rust layer analysis, and electrochemical measurements. Samples were ground with 800# sandpaper, cleaned with alcohol, and dried before being used for CCT. The CCT procedure is as follows: (1) the original samples were weighed; (2) the sample surface ($15 \, mm \times 15 \, mm$) was wetted with $80 \, \mu L \, cm^{-2}$ of 0.3% NaCl solution (wt%); (3) the samples were held in a constant temperature and humidity chamber at 25 °C, 60% RH for 24 h; (4) the dried samples were reweighed; (5) the samples were washed with deionized water to avoid the accumulation of NaCl and dried again; (6) the steps (2)–(5) were repeated. Six parallel samples of each weathering steel were prepared to improve the accuracy of the experiment. The experimental period lasted 30 CCT.

Rust layer characterization

The rust layer was observed by SEM (Hitachi S–3400), and the element distribution of the rust layer was determined by EDS. The descaling solution (500 mL hydrochloric acid + 500 mL deionized water + 3.5 g hexamethylenetetramine) was used to remove the rust layer generated on the samples at 30 CCT[44]. They were then cleaned with alcohol, dried, and weighed with a balance. In order to determine the error caused by substrate dissolution in the descaling solution, a blank sample of the same size for each steel was used for weight loss correction. The blank sample was placed in the descaling solution with the same time, and the weight loss was recorded as m_1. The corrosion loss rate was calculated from the following equation:

$$V = \frac{m_0 - m_t - m_1}{st} \qquad (4)$$

where V is the corrosion loss rate (mg cm^{-2} CCT), s is the exposed area (cm^2), t is time (CCT), m_0 is the initial weight of the samples (mg) and m_t is the weight loss caused by substrate loss. The rust layer was scraped off, and its composition was studied through XRD (PCX D/Max–2500) and XPS (Thermo Scientific ESCALAB 250XI). XRD scans were obtained over the 2θ range of 10–70°, with a step size of 0.02° and step time of 2 s. XRD spectra were semi-quantitatively analyzed using the RIR method to determine the phase content[45]. The binding energy of XPS was adjusted for the charging effect by referencing the C1s peak (284.8 eV). The composition of the inner and outer rust layer was studied using MicroRaman spectrometer (Horiba LabRAM Evolution). The Raman shift range was $200–1400 \, cm^{-1}$, the spectrum acquisition time was 10 s and the laser wavelength was 532 nm. Phases in the rust layer were identified on the basis of the peak positions in previous studies[36,46–48]. The rust layer was analyzed using TEM (FEI TECNAL G2 S–TWIN F20) accompanied by selected area electron diffraction (SAED).

Electrochemical measurement

The Potentiodynamic polarization curve and EIS of rusted steel were conducted on an electrochemical workstation (PARSTAT 3000A–DX). A conventional three-electrode system was used, with the working electrode being rusted steel, the reference electrode being a saturated calomel electrode, and the counter electrode being a platinum electrode. The test solution was 0.3 wt% NaCl solution. The potentiodynamic polarization curve was performed at a scan rate of $1 \, mV \, s^{-1}$, from $-1.5 \, V$ to $1.5 \, V$. The corrosion potential (E_{corr}) and corrosion current density (i_{corr}) were determined using the Tafel extrapolation method[22]. The frequency range of EIS measurements was 100 kHz to 10 mHz, and the amplitude was 10 mV. The EIS data were fitted and analyzed using Zsimpwin software. All measurements were performed at room temperature (~25 °C) and repeated at least three times to ensure reproducibility.

Data availability

Available from the corresponding author upon reasonable request.

References

1. Zhang, T. et al. On how the corrosion behavior and the functions of Cu, Ni and Mo of the weathering steel in environments with different NaCl concentrations. *Corros. Sci.* **192**, 109851 (2021).
2. Yu, Q. et al. Layer-by-layer investigation of the multilayer corrosion products for different Ni content weathering steel via a novel Pull-off testing. *Corros. Sci.* **195**, 109988 (2022).
3. Yang, X. et al. A new understanding of the effect of Cr on the corrosion resistance evolution of weathering steel based on big data technology. *J. Mater. Sci. Technol.* **104**, 67–80 (2022).
4. Kim, S.-H., Kim, H. & Kim, N. J. Brittle intermetallic compound makes ultrastrong low-density steel with large ductility. *Nature* **518**, 77–79 (2015).
5. Gutierrez-Urrutia, I., Shibata, A. & Tsuzaki, K. Microstructural study of microbands in a Fe-30Mn-6.5Al-0.3C low-density steel deformed at cryogenic temperature by combined electron channeling contrast imaging and electron backscatter diffraction. *Acta Mater.* **233**, 117980 (2022).
6. An, Y. F. et al. Precipitation transformation pathway and mechanical behavior of nanoprecipitation strengthened Fe-Mn-Al-C-Ni austenitic low-density steel. *J. Mater. Sci. Technol.* **174**, 157–167 (2024).
7. Hu, B. et al. Ultrahigh tensile strength achieved in a lightweight medium Mn steel via prominent work hardening. *J. Mater. Sci. Technol.* **145**, 156–164 (2023).
8. Ko, K. K. et al. A feasible route to produce 1.1 GPa ferritic-based low-Mn lightweight steels with ductility of 47%. *J. Mater. Sci. Technol.* **117**, 225–237 (2022).
9. Kim, C. et al. A new strengthening mechanism driven by disruptive shear and solute segregation during warm rolling in 1.4 GPa class 12.5 wt% Al added-FeMnC ultra-lightweight steel. *J. Mater. Sci. Technol.* **157**, 174–188 (2023).
10. Chen, S., Rana, R., Haldar, A. & Ray, R. K. Current state of Fe-Mn-Al-C low density steels. *Prog. Mater. Sci.* **89**, 345–391 (2017).
11. Chen, X. H., Dong, J. H., Han, E. H. & Ke, W. Effect of Al alloying on corrosion performance of steel. *Corros. Eng., Sci. Technol.* **42**, 224–231 (2007).
12. Xu, X. et al. Optimizing the resistance of Ni-advanced weathering steel to marine atmospheric corrosion with the addition of Al or Mo. *Constr. Build. Mater.* **279**, 122341 (2021).
13. Fajardo, S., Llorente, I., Jiménez, J. A., Bastidas, J. M. & Bastidas, D. M. Effect of Mn additions on the corrosion behaviour of TWIP Fe-Mn-Al-Si austenitic steel in chloride solution. *Corros. Sci.* **154**, 246–253 (2019).
14. Cho, D. H., Lee, B. W., Park, J. Y., Cho, K. M. & Park, I. M. Effect of Mn addition on corrosion properties of biodegradable Mg-4Zn-0.5Ca-xMn alloys. *J. Alloy. Compd.* **695**, 1166–1174 (2017).
15. Jia, J., Wu, W., Cheng, X. & Zhao, J. Ni-advanced weathering steels in Maldives for two years: corrosion results of tropical marine field test. *Constr. Build. Mater.* **245**, 118463 (2020).

16. Tian, H. et al. Electrochemical corrosion, hydrogen permeation and stress corrosion cracking behavior of E690 steel in thiosulfate-containing artificial seawater. *Corros. Sci.* **144**, 145–162 (2018).

17. Hara, S., Kamimura, T., Miyuki, H. & Yamashita, M. Taxonomy for protective ability of rust layer using its composition formed on weathering steel bridge. *Corros. Sci.* **49**, 1131–1142 (2007).

18. Kamimura, T., Hara, S., Miyuki, H., Yamashita, M. & Uchida, H. Composition and protective ability of rust layer formed on weathering steel exposed to various environments. *Corros. Sci.* **48**, 2799–2812 (2006).

19. Morcillo, M., Díaz, I., Cano, H., Chico, B. & de la Fuente, D. Atmospheric corrosion of weathering steels. Overview for engineers. Part II: Testing, inspection, maintenance. *Constr. Build. Mater.* **222**, 750–765 (2019).

20. Sugimoto, I. & Kita, K. Evaluation of applicability for Ni-advanced weathering steels and bridge high-performance steels to railway steel bridges. *Q. Rep. RTRI* **51**, 33–37 (2010).

21. Diaz, I. et al. Atmospheric corrosion of Ni-advanced weathering steels in marine atmospheres of moderate salinity. *Corros. Sci.* **76**, 348–360 (2013).

22. McCafferty, E. Validation of corrosion rates measured by the Tafel extrapolation method. *Corros. Sci.* **47**, 3202–3215 (2005).

23. Ci, W. et al. Effect of Zn on mechanical and corrosion properties of Mg-Sc-Zn alloys. *J. Mater. Sci. Technol.* **158**, 31–42 (2023).

24. Li, D. G., Wang, J. D., Chen, D. R. & Liang, P. Influences of pH value, temperature, chloride ions and sulfide ions on the corrosion behaviors of 316L stainless steel in the simulated cathodic environment of proton exchange membrane fuel cell. *J. Power Sources* **272**, 448–456 (2014).

25. Freire, L., Carmezim, M. J., Ferreira, M. G. S. & Montemor, M. F. The electrochemical behaviour of stainless steel AISI 304 in alkaline solutions with different pH in the presence of chlorides. *Electrochim. Acta* **56**, 5280–5289 (2011).

26. Huang, Y. & Zhu, Y. Hydrogen ion reduction in the process of iron rusting. *Corros. Sci.* **47**, 1545–1554 (2005).

27. Xiong, X. L., Zhou, Q. J., Li, J. X., Volinsky, A. A. & Su, Y. J. Cathodic over-potential and hydrogen partial pressure coupling in hydrogen evolution reaction of marine steel under hydrostatic pressure. *Electrochim. Acta* **247**, 1019–1029 (2017).

28. Alcántara, J. et al. Marine atmospheric corrosion of carbon steel: a review. *Materials* **10**, 406 (2017).

29. Morcillo, M., Díaz, I., Cano, H., Chico, B. & de la Fuente, D. Atmospheric corrosion of weathering steels. Overview for engineers. Part I: basic concepts. *Constr. Build. Mater.* **213**, 723–737 (2019).

30. Lu, Q. et al. Corrosion evolution and stress corrosion cracking of E690 steel for marine construction in artificial seawater under potentiostatic anodic polarization. *Constr. Build. Mater.* **238**, 117763 (2020).

31. Sun, M., Pang, Y., Du, C., Li, X. & Wu, Y. Optimization of Mo on the corrosion resistance of Cr-advanced weathering steel designed for tropical marine atmosphere. *Constr. Build. Mater.* **302**, 124346 (2021).

32. Suzuki, S. et al. A new method for describing the atomic-scale structure of rusts formed on the iron based alloy surfaces. *ISIJ Int.* **43**, 366–372 (2003).

33. Kimura, M., Suzuki, T., Shigesato, G., Kihira, H. & Suzuki, S. Characterization of nanostructure of rusts formed on weathering steel. *ISIJ Int.* **42**, 1534–1540 (2002).

34. Kimura, M., Kihira, H., Ohta, N., Hashimoto, M. & Senuma, T. Control of Fe(O,OH)6 nano-network structures of rust for high atmospheric-corrosion resistance. *Corros. Sci.* **47**, 2499–2509 (2005).

35. Nishimura, T. Corrosion resistance of Si-Al-bearing ultrafine-grained weathering steel. *Sci. Technol. Adv. Mater.* **9**, 013005 (2008).

36. Wu, W., Cheng, X., Hou, H., Liu, B. & Li, X. Insight into the product film formed on Ni-advanced weathering steel in a tropical marine atmosphere. *Appl. Surf. Sci.* **436**, 80–89 (2018).

37. Mizoguchi, T., Ishii, Y., Okada, T., Kimura, M. & Kihira, H. Magnetic property based characterization of rust on weathering steels. *Corros. Sci.* **47**, 2477–2491 (2005).

38. Kihira, H. et al. Creation of alloy design concept for anti air-born salinity weathering steel. *Zairyo-to-Kankyo* **49**, 30–40 (2000).

39. Lei, X. et al. Porous MnO as efficient catalyst towards the decomposition of Li2CO3 in ambient Li-air batteries. *Electrochim. Acta* **280**, 308–314 (2018).

40. Esmaeilnejad, A., Mahmoudi, P., Zamanian, A. & Mozafari, M. Synthesis of titanium oxide nanotubes and their decoration by MnO nanoparticles for biomedical applications. *Ceram. Int.* **45**, 19275–19282 (2019).

41. Jia, J., Cheng, X., Yang, X., Li, X. & Li, W. A study for corrosion behavior of a new-type weathering steel used in harsh marine environment. *Constr. Build. Mater.* **259**, 119760 (2020).

42. Burger, E., Fénart, M., Perrin, S., Neff, D. & Dillmann, P. Use of the gold markers method to predict the mechanisms of iron atmospheric corrosion. *Corros. Sci.* **53**, 2122–2130 (2011).

43. Hao, L., Zhang, S., Dong, J. & Ke, W. Evolution of atmospheric corrosion of MnCuP weathering steel in a simulated coastal-industrial atmosphere. *Corros. Sci.* **59**, 270–276 (2012).

44. Liu, H. et al. Essential role of element Si in corrosion resistance of a bridge steel in chloride atmosphere. *Corros. Sci.* **173**, 108758 (2020).

45. Hubbard, C. R. & Snyder, R. L. RIR - measurement and use in quantitative XRD. *Powder Diffr.* **3**, 74–77 (1988).

46. Fan, Y. et al. Evolution of rust layers on carbon steel and weathering steel in high humidity and heat marine atmospheric corrosion. *J. Mater. Sci. Technol.* **39**, 190–199 (2020).

47. Demoulin, A. et al. The evolution of the corrosion of iron in hydraulic binders analysed from 46- and 260-year-old buildings. *Corros. Sci.* **52**, 3168–3179 (2010).

48. Neff, D., Bellot-Gurlet, L., Dillmann, P., Reguer, S. & Legrand, L. Raman imaging of ancient rust scales on archaeological iron artefacts for long-term atmospheric corrosion mechanisms study. *J. Raman Spectrosc.* **37**, 1228–1237 (2006).

Author contributions
Y.H.T.: Data curation, Conceptualization, Investigation, Writing-original draft, Formal analysis. Y.X.G.: Investigation, Writing-review & editing. P.F.J.: Investigation, editing. B.L.: Investigation, editing. C.Q.X.: Supervision, Conceptualization, Investigation. S.Z.Z.: Investigation, Formal analysis. J.S.Z.: Writing-review & editing. X.Y.Z.: Visualization, Investigation. R.R.L.: Supervision, Conceptualization.

Competing interests
The authors declare no competing interests.

Additional information
Supplementary information The online version contains supplementary material available at https://doi.org/10.1038/s41529-024-00450-0.

Correspondence and requests for materials should be addressed to Chaoqun Xia, Xinyu Zhang or Riping Liu.

Reprints and permissions information is available at http://www.nature.com/reprints